Check for updates

LASER & PHOTONICS REVIEWS
www.lpr-journal.org

Boosting Applications with High-Performance Near-Infrared Phosphor-Converted Light-Emitting Diodes

Ruiyang Li, Yongfu Liu, Chen Jin, Liangliang Zhang, Jiahua Zhang, Xiao-Jun Wang,* Guoxin Chen, and Jun Jiang**

Near-infrared (NIR) phosphor-converted (pc) light-emitting diodes (LEDs) are gaining popularity as smart NIR spectroscopy light sources. However, the low wall-plug efficiency (WPE) of NIR pc-LEDs has limited their applications due to the comprehensive properties of external quantum efficiencies (EQEs) and thermal stability for NIR phosphors. In this study, a simple strategy is presented to achieve high-performance NIR phosphors by breaking the d–d parity forbidden transitions of Cr^{3+} in the garnet host by introducing asymmetric vibrations via lattice distortions. The achieved EQE is as high as 44% at room temperature and maintains >98% of the initial EQE at 150 °C, demonstrating excellent thermal stability. Notably, these NIR phosphors enable unprecedented NIR pc-LEDs with a record WPE of 26% driven at 100 mA. Consequently, the application of NIR pc-LEDs is expanded to new areas such as real-time heart rate monitoring and fingerprint recognition.

1. Introduction

Near-infrared (NIR) spectroscopy is a widely -used technology in fields such as biomedical imaging,[1–3] photodynamic therapy,[4] non-destructive inspection,[5–7] night-vision systems,[8] and agriculture.[9] To support the growing demand for NIR applications, there is a need to develop more efficient, compact, and broader band emission light sources. Various types of NIR light-emitting diodes (LEDs) using perovskite,[10,11] quantum dots,[12] and organic[12,13] or inorganic phosphors[14–20] have been developed, with particular interest in NIR phosphor-converted LEDs (NIR pc-LEDs) that use blue LED chips and NIR emissive phosphors due to their high efficiency.[12,21–23] Efforts have focused on controlling and enhancing NIR emissions from 700 to 1000 nm, resulting in broadband and efficient NIR pc-LEDs with wall-plug efficiency (WPE,[24] the ratio of the output NIR power over the input electric power) exceeding 23%.[22,23] However, the stability of NIR phosphors remains a key issue in practical applications,[12] as does the external quantum efficiency (EQE) and thermal stability.[25–27] Strategies to improve efficiency and stability are currently being explored, and success in this regard would represent a significant milestone in the commercialization of NIR pc-LEDs.

The key properties of EQE are determined by both internal quantum efficiency (IQE) and absorbance (Abs), i.e., EQE = IQE × Abs.[8,28] This highlights the importance of controlling both IQE and Abs in enhancing the performance of both NIR phosphors and NIR pc-LED devices. Current strategies aimed at improving NIR mainly focus on the selection of higher-quality materials such as garnets[8,23,28–31] and fluorides,[32] as well as identifying new materials like ceramics and phosphor glass[33–35] with broader and brighter intrinsic NIR emission. However, we have developed a different approach to this issue, which we call "breaking forbidden transition". Our approach is motivated by the observation that the light emitter in NIR is strongly dependent on host materials. For example, Cr^{3+} is widely investigated because the optically active d-electron shell strongly depends on the crystal field in hosts and therefore shows tunable NIR emission. However, the d–d transition is parity forbidden due to inversion symmetry,[36] making the Abs generally small. To break this symmetry, the 3*d* parity forbidden transition is usually broken by introducing the 3*d*4*p* and 3*d*4*f* odd-parity crystal field through lattice distortions and asymmetric vibrations.[23,28–30,37] Although lattice distortion enhances Abs, it also lowers IQE and thermal stability.[34]

Herein, we demonstrate the "breaking forbidden transition" strategy to enhance both Abs and IQE, as well as the excellent thermal stability in Cr^{3+} -activated Gadolinium–Gallium garnet (GGG: Cr^{3+}). GGG:Cr^{3+} is a promising material for

R. Li, Y. Liu, C. Jin, G. Chen, J. Jiang
Ningbo Institute of Materials Technology & Engineering
Chinese Academy of Sciences
Ningbo 315201, P. R. China
E-mail: liuyongfu@nimte.ac.cn; jjun@nimte.ac.cn
R. Li
University of Chinese Academy of Sciences
Beijing 100049, P. R. China
L. Zhang, J. Zhang
State Key Laboratory of Luminescence and Applications
Changchun Institute of Optics
Fine Mechanics and Physics
Chinese Academy of Sciences
Changchun 130033, P. R. China
X.-J. Wang
Department of Physics
Georgia Southern University
Statesboro, GA 30460, USA
E-mail: xwang@georgiasouthern.edu

The ORCID identification number(s) for the author(s) of this article can be found under https://doi.org/10.1002/lpor.202300608

DOI: 10.1002/lpor.202300608

 © 2023 Wiley-VCH GmbH

photomorphogenic LEDs because of its most suitable photoluminescence (PL), but its IQE is only 30% due to parity forbidden transitions of Cr^{3+} in the garnet lattice.[38] In this work, we introduce the smaller Al to substitute Ga. The preferred distribution of Al distorts the garnet and introduces asymmetric lattice vibrations that break the Cr^{3+} parity-forbidden transitions and enhance Abs. Furthermore, optimizing the Cr^{3+} concentration and sintering technology greatly improved IQE to over 85%. Correspondingly, the optimized sample showed an EQE of 44.0% ± 0.2% at ambient temperature, and EQE at 150 °C maintained 98.1% of the initial value. To our knowledge, these results demonstrate the best combination of high efficiency and excellent thermal stability. Outstandingly, these phosphors enable the fabrication of NIR pc-LEDs with an unprecedented WPE of 26.0%, a record reported to date. This allows us to extend the applications of NIR pc-LEDs to new areas of real-time heart rate monitoring and fingerprint recognition for the first time. The easy synthesis conditions, sintering in the ambient atmosphere, and excellent chemical and environmental stability facilitate reproducibility and fabrication. Therefore, we believe that the developed NIR phosphors may be a promising commercial candidate for NIR pc-LEDs.

2. Results and Discussion

2.1. Structure and Morphology

Garnet, a cubic crystal structure, has the chemical formula $C_3A_2D_3O_{12}$, where C, A, and D are connected with 8, 6, and 4 oxygen atoms, respectively, denoting the dodecahedral, octahedral, and tetrahedral site with point symmetries.[8] GGG shows the chemical composition of $Gd_3Ga_2Ga_3O_{12}$ as well as the dodecahedral GdO8, octahedral Ga(I)O6, and tetrahedral Ga(II)O4 sites (Figure S1, Supporting Information). It is generally accepted that Cr^{3+} occupies the octahedral Ga(I)O6 site.[8,23,36] We also demonstrate the Cr^{3+} occupation via the Rietveld refinement of the powder X-ray diffraction (XRD) patterns. The refined results for Cr^{3+} presenting at the octahedral Ga(I)O6 site (R_{wp} = 6.40%, R_p = 4.84%, and χ^2 = 1.68, Figure S2a, Supporting Information) are better convergent than those for Cr^{3+} presenting at the tetrahedral Ga(II)O4 site (R_{wp} = 8.76%, R_p = 7.19%, and χ^2 = 3.13, Figure S2b, Supporting Information).

The Cr^{3+} PL is from the octahedral CrO6 site surrounded by six oxygen atoms as the nearest neighbor anions.[36] The six Ga(II) atoms are the nearest neighbor cations around Cr^{3+} as well, which indicates that modifying Ga(II) sites and Ga(II)O4 tetrahedra should be a useful strategy to tune the Cr^{3+} PL property. Here, we introduce Al to substitute Ga to modify both the Ga(I)O6 octahedra and the Ga(II)O4 tetrahedra. Based on the common molecular formula of $C_3A_2D_3O_{12}$, theoretically, the Al distribution at the octahedral and the tetrahedra sites should be 40% and 60%, respectively. For instance, $Gd_3Ga_4AlO_{12}$ (GGAG) could be $Gd_3(Ga_{0.8}Al_{0.2})_2(Ga_{0.8}Al_{0.2})_3O_{12}$ and the Al/Ga ratio at the tetrahedral site is 1/4. The nearest neighbor cations of Cr^{3+} could change from [6Ga(II)] to [4.8Ga(II)+1.2Al(II)] in theoretical (**Figure 1a,b**). Factually, the Rietveld refinement results of the XRD data of GGAG reveal that Al at the octahedral and the tetrahedral sites are 70.8% and 29.2%, respectively (Table S1, Supporting Information). That is, GGAG is actual to be $Gd_3(Al_{0.354}Ga_{0.546}Cr_{0.1})_2(Al_{0.097}Ga_{0.903})_3O_{12}$. So from GGG: Cr^{3+} to GGAG:Cr^{3+} the nearest neighbor cations of Cr^{3+} change from [6Ga(II)] to [5.42Ga(II)+0.58Al(II)] in experimental (Figure 1c), and this could distort the local structure around Cr^{3+} and break the forbidden transition for enhancing Cr^{3+} absorption. These results further reveal that the smaller Al is non-randomly distributed and prefers the larger octahedral site rather than the smaller tetrahedral site (Figure 1c and Figure S3, Supporting Information). The abnormal occupation is widely observed in the Al-Ga garnet solid solutions.[39,40] Because the covalency of the Al—O bond is weaker than that of the Ga—O bond, the preferred Al at the larger octahedral site relaxes the cation-cation repulsion and leads to the lower energy as well as a stable structure.[30,39,40] Naturally, the preferred and non-random occupation twists both the octahedra and the tetrahedra. From GGG:Cr^{3+} to GGAG:Cr^{3+}, the distortion in both octahedral and tetrahedral environments can be observed through changes in bond angles and bond lengths (Figure S4 and Tables S2 and S3, Supporting Information). Similar results, inducing octahedral distortion to enhance NIR emission, are also observed in the Cr-doped $Ca_3(Al, Sc)_2Ge_3O_{12}$ garnet.[14] Although it is different to determine the distortion index, it is not zero. Thus, asymmetric media from the distorted both octahedra and tetrahedra environments and the distortion of the nearest neighbor cations around Cr^{3+} are expected to break the Cr^{3+} parity forbidden transitions and enhance its absorption.

The Al modification into the garnet crystal structure is directly observed by the high-angle annular dark-field (HAADF)-scanning transmission electron microscope (STEM) tomography at an atomic-scale resolution. GGG shows a typical cubic structure projected along the [001] direction, and peaks in the curves from the line scans correspond to Gd and Ga atomic columns in the HAADF-STEM image (Figure 1d; Figure S5a, Supporting Information). The octahedral sites are only occupied by Ga seen from the ordered Ga distribution. However, the ordered octahedral sites are broken due to the preferred occupation of Al in the GGAG matrix. The contrast curves from the line scans evidence that the structural distributions of Ga and Al are inhomogeneous and disordered in the HAADF-STEM image of GGAG (Figure 1e; Figure S5b, Supporting Information). Asymmetric lattice vibrations from the disordered octahedra are carefully estimated by the Raman spectra. For the GGG matrix, the vibration frequency ranges of 300–460 cm^{-1} and 650–850 cm^{-1} are from the Ga(I)O6 octahedra and the Ga(II)O4 tetrahedra, respectively (Figure S6, Supporting Information). The lighter Al than Ga leads to a stronger vibration. When the matrix evolves from GGG into GGAG, thus the vibrational peaks shift to the high frequency for both octahedra (from 354.7 to 358.0 cm^{-1}) and tetrahedra (from 741.7 to 746.9 cm^{-1}). Asymmetries from the distorted octahedra lead to the broader vibration band, thus the full width at half maximum (FWHM) of the octahedral vibration broadens from 12.5 to 14.8 cm^{-1}. Similar phenomena are also carefully observed in the distorted tetrahedra, where asymmetries lead to broader vibration as well. The incorporated asymmetric media from both octahedra and tetrahedra break the forbidden parity of the Cr^{3+} d–d transition. Thus, the Abs to blue light associated to the $^4A_{2g} \rightarrow {}^4T_{1g}$ transition of Cr^{3+} is strengthened, demonstrated by the diffuse reflectance (DR) spectra (Figure S7, Supporting Information).

© 2023 Wiley-VCH GmbH

18638899, 2024, 3, Downloaded from https://onlinelibrary.wiley.com/doi/10.1002/lpor.202300608 by Cas-Changchun Institute Of Optics, Fine Mechanics And Physics, Wiley Online Library on [18/04/2024]. See the Terms and Conditions (https://onlinelibrary.wiley.com/terms-and-conditions) on Wiley Online Library for rules of use; OA articles are governed by the applicable Creative Commons License

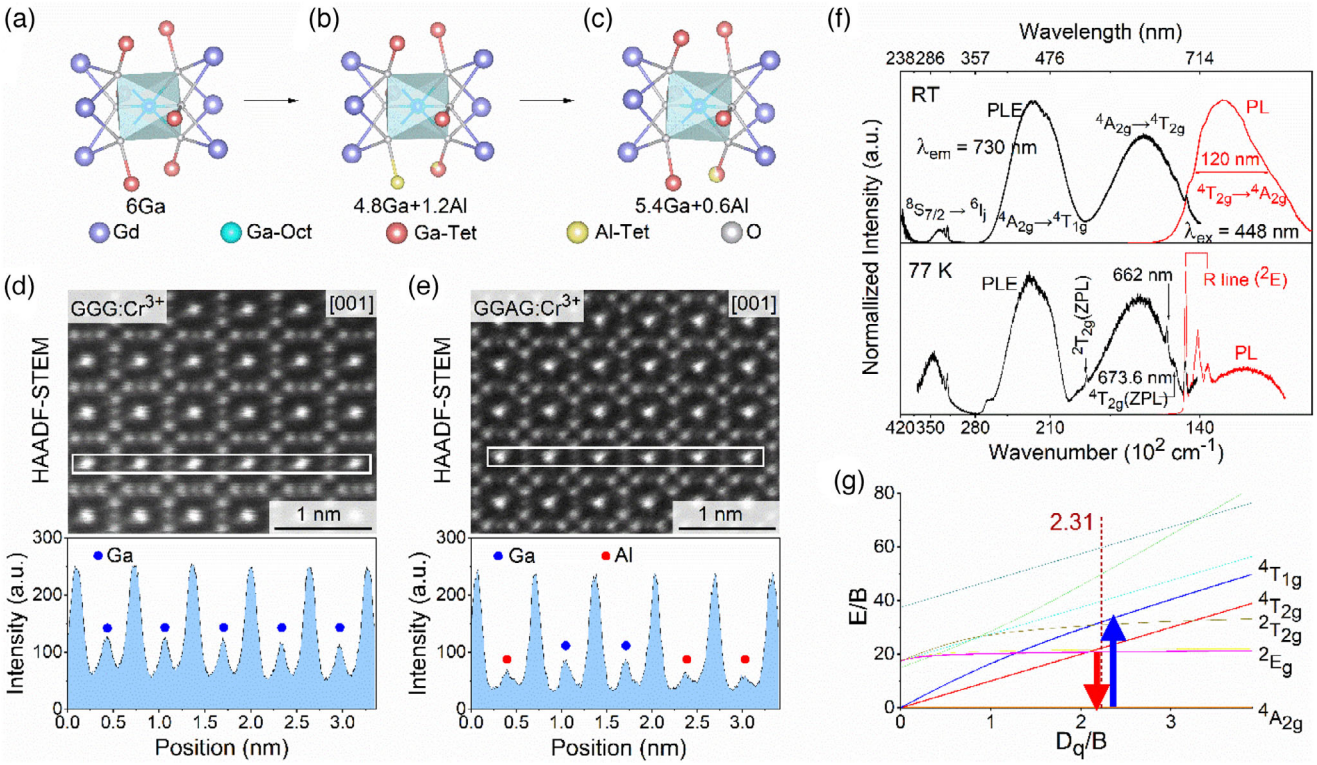

Figure 1. Structural, morphological, and luminescence. a–c) Coordinated atoms around the octahedral site and Ga/Al distributions in GGG and GGAG in theoretical and experimental. d,e) HAADF-STEM images and line scans of Gd, Ga, and Al columns from GGG: Cr^{3+} and GGAG:Cr^{3+} particles. f) PLE and PL spectra of GGAG:20%Cr^{3+} measured at RT and 77 K. g) Crystal field parameter and Tanabe-Sugano energy levels of Cr^{3+} ($3d^3$) in the octahedral coordination in GGAG.

We note that the vibrational frequency from 100 to 300 cm^{-1} is mainly attributed to the GdO8 dodecahedra and several splits and sharp vibrational peaks usually indicate the Gd-Ga anti-site defects that lower the symmetry of the dodecahedral vibration bands.[29] Because the ionic radius (r) of Ga^{3+} (r = 0.62 Å, six-coordinated) is close to that of Gd^{3+} (r = 0.938 Å, six-coordinated) and Ga is easier to present at the Gd site. The ionic radius of the Al^{3+} (r = 0.535 Å, six-coordinated) is much smaller than that of Gd^{3+}. This big difference means that Al^{3+} is hard to present at the GdO8 site.[41] Thus, the anti-site defects may decrease, and the symmetry increases evidenced by the smooth vibrational spectra in GGAG (Figure S6, Supporting Information). The preferred occupation of Al at the octahedra distorts both the octahedra and the tetrahedra, resulting in asymmetries to break the parity forbidden transitions of the Cr^{3+}. The Al substitution to Ga may depress the anti-site defect and then enable a high intrinsic luminescence. These are evidenced by the enhancement of both the IQE and the Abs (Figure S8, Supporting Information). The IQE and EQE of GGAG:Cr^{3+} reach 54±1.0% and 37±0.9%, respectively, which is greatly higher than the result (IQE = 30%) of GGG:Cr^{3+} reported by Zabiliūtė et al.[38] It is carefully found that the increase in Abs is bigger than that in IQE when the host evolves from GGG to GGAG. This may indicate that the preferred Al substitution plays a dominant role in introducing asymmetries to break forbidden transitions other than depressing anti-site defects.

2.2. Luminescence Mechanism

The investigations of Al on the GGG host are based on the powder samples with the nominal composition of $Gd_3Ga_{4-x}AlCr_xO_{12}$ (GGAG:$x$$Cr^{3+}$, x = 5–30%) that sintered at 1650 °C in an air atmosphere. This sintering technology enables to achieve the single garnet phase, which simplifies the revealing of the Cr^{3+} PL mechanism. Cr^{3+} (r = 0.615 Å, six-coordinated) is very close to Ga^{3+} (r = 0.62 Å), thus all the samples keep the single garnet phase (Figure S9, Supporting Information) and show the same luminescence (Figure 1f). The optimized sample is GGAG:20%Cr^{3+} (Figure S10, Supporting Information). The powders have particle sizes of ≈3–10 µm in the scanning electron microscope (SEM) images (Figure S11b, Supporting Information). The elements Gd, Al, Ga, O, and Cr are almost homogeneous in the SEM energy dispersive X-ray spectroscopy (EDS) mapping images (Figure S11a,c, Supporting Information). The homogeneous cathodoluminescence (CL) is observed in the SEM-CL image. The CL spectra for different points show the same peak at 730 nm and their FWHMs are ≈105 nm, which are similar to the PL spectra.

In Figure 1f, GGAG:20%Cr^{3+} shows two strong photoluminescence excitation (PLE) bands centered at 448 and 620 nm that are from the spin-allowed Cr^{3+} transitions of $^4A_{2g} \rightarrow {}^4T_{1g}$ and $^4A_{2g} \rightarrow {}^4T_{2g}$, respectively.[8,42] The weak PLE band ≈310 nm is from the $^8S_{7/2} \rightarrow {}^6I_j$ transition of Gd^{3+}. These are consistent

© 2023 Wiley-VCH GmbH

18638899, 2024, 3, Downloaded from https://onlinelibrary.wiley.com/doi/10.1002/lpor.202300608 by Cas-Changchun Institute Of Optics, Fine Mechanics And Physics, Wiley Online Library on [18/04/2024]. See the Terms and Conditions (https://onlinelibrary.wiley.com/terms-and-conditions) on Wiley Online Library for rules of use; OA articles are governed by the applicable Creative Commons License

with the DR spectra. Under the blue light excitation, the PL spectrum only shows a broad band peaked at 730 nm with a FWHM of 120 nm from the $^4T_{2g} \rightarrow {}^4A_{2g}$ transition at room temperature (RT). From GGG: xCr^{3+} to GGAG: xCr^{3+} (x = 5–30%) the emission peak wavelength shifts from 735 to 730 nm and the R-line increases obviously at RT (Figures S12 and S13b, Supporting Information), but the spectral shape is nearly independent of the Cr^{3+} concentration. These phenomena indicate that the crystal field splitting is slightly strengthened when the bigger Ga^{3+} is substituted by the smaller Al^{3+}, which is called the "crystal-field engineering".[43] The crystal field effects can also be observed from the PLE and PL spectra of GGG:20%Cr^{3+} and GGAG:20%Cr^{3+} at 77 K (Figure S13a, Supporting Information).

Sharp peaks identified at a low temperature (77 K) reveal the luminescence mechanism.[44–46] For GGG:20%Cr^{3+} the sharp peaks detected both in the PLE and PL spectra at the same wavelength region are the zero-phonon line (ZPL) of the ^2E_g (R-lines) energy level (Figure S13a, Supporting Information), which is 692.6 nm (14 438 cm^{-1}) in the PLE spectrum, and the tiny peak at 675.2 nm (14 810 cm^{-1}) represents the ZPL of the $^4T_{2g}$ energy level. For GGAG:20%Cr^{3+} the ZPL of the ^2E_g and $^4T_2$ energy level is 691.0 nm (14 472 cm^{-1}) and 673.6 nm (14 846 cm^{-1}) in the PLE spectrum (Figure 1f; Figure S13a, Supporting Information). Therefore, from GGG:20%Cr^{3+} to GGAG:20%Cr^{3+}, the R line shifts from 14 438 to 14 453 cm^{-1} (ΔE = 15 cm^{-1}), and the $E_0(^4T_2)$ shifts from 14 810 to 14 846 cm^{-1} (ΔE = 36 cm^{-1}). These results again illustrate the enhanced crystal field effect. Moreover, For GGAG:20%Cr^{3+} the first phonon satellite of the $^4T_{2g}$ energy level is observed at 662 nm (15 106 cm^{-1}) in the PLE spectrum. The estimated phonon energy is ≈260 cm^{-1}, which is close to the anti-Stokes shift in Raman spectra (vibrational peak at about 230 cm^{-1}). The tiny sharp peak at 533.8 nm (18 734 cm^{-1}) is the ZPL of the $^2T_{2g}$ energy level. The energy difference between the ^2E_g R-line and the $^4T_{2g}$ ZPL is 374 cm^{-1} in GGAG:Cr^{3+}, which is close to the value of 372 cm^{-1} in GGG:Cr^{3+}, meaning a strong spin-orbit coupling (SOC) between the ^2E_g and $^4T_{2g}$ states.[36]

Based on these results at 77 K and RT, the crystal field parameters are calculated by the Tanabe-Sugano formulas (Tables S4 and S5, Supporting Information).[45] The crystal field Dq and the Racah electron repulsion parameter B are calculated to be 1484.6 and 642.2 cm^{-1}, respectively. The value of Dq/B is 2.31, and then the energy diagram of Cr^{3+} in the GGAG host is illustrated (Figure 1g). Electrons pumped to the $^4T_{1g}(^4F)$ states (blue arrow, $^4A_{2g} \rightarrow {}^4T_{1g}$) will relax to the $^4T_{2g}(^4F)$ state. The broadband emission is from the $^4T_{2g} \rightarrow {}^4A_{2g}$ transition (red arrow). Sharp peaks at 692, 711, and 727 nm are from the R-line ($^2E_g \rightarrow {}^4A_{2g}$) and its long-wave phonon sidebands (PL@77 K).[36,45,46] The energy difference between sidebands of 692 and 711 nm of ^2E_g is ≈360 cm^{-1}, which is close to the Stokes shift in Raman spectra (vibrational peak at about 355 cm^{-1}). These indicate that the octahedral vibrations play a dominant effect, including Stokes and anti-Stokes shifts, on the luminescence of the $^4T_{2g}$ and ^2E_g states. The small energy difference between the $^4T_{2g}$ and ^2E_g states results in the strong SOC effect, and thermalization of these two states is allowed. The emitting $^4T_{2g}$ and ^2E_g states are mixed by the SOC and electron-phonon coupling (EPC).[8,36] The ^2E_g emission is identified only at a low temperature (77 K). At a high temperature, only the $^4T_{2g}$ emission is observed (PL@RT) due to the strong SOC and EPC effects. Thus, all the fluorescence decay kinetics show almost the single exponential behavior monitored at the $^4T_{2g}$ or ^2E_g states at RT (693, 715, or 730 nm, Figure S14, Supporting Information).

2.3. Efficiency Enhancement

We further enhance the luminescence via a simple sintering technology. We add the H_3BO_3 flux and the sintering temperature drops from 1650 to 1350 °C due to the promoted reactivity of raw materials, which is more beneficial to reduce the energy consumption and the production cost. The optimal sample is GGAG:10%Cr^{3+} with 3wt% H_3BO_3 confirmed by orthogonal experiments. The achieved luminescence is much better than the obtained by the sintering technology (Figure S15, Supporting Information). Based on the simple technology, we enhance the Abs from 31 ± 0.2‰ to 57 ± 0.5‰ by increasing the Cr^{3+} concentration from 1% to 12%, at which the Abs almost reaches the saturation (**Figure 2a**). We try our best to explain the reason for adding flux reducing the optimal concentration of Cr^{3+}, which could be the Cr^{3+} evaporation at a high temperature. The evaporation could be weakened when the sintering temperature declines from 1650 to 1350 °C by adding the H_3BO_3 flux. The Cr^{3+} could be easy to reach saturation and this is the possible reason why the optimal Cr^{3+} concentration is lowered to 10%. On the other hand, the IQE rises from 83 ± 1.4% to 86 ± 1.6% and then falls when Cr^{3+} reaches 6%, which is consistent with the regular fluorescent lifetime dependent on the Cr^{3+} concentration (Figure S16, Supporting Information). The lifetime lengthens from 201.3 (1%Cr^{3+}) to 210.2 µs (6%Cr^{3+}) and then shortens to 164.9 µs (16%Cr^{3+}) (Figure 2b). These are reasonable and well-known as the concentration quenching effect due to the strengthened non-radiative relaxation between Cr^{3+}-Cr^{3+} via energy migration (Figure 2c). The critical distance (R_c) of the concentration quenching is calculated to be 17.08 Å based on the refined volume of GGAG:6%Cr^{3+} (Figure S17 and Tables S6–S8, Supporting Information). Combining the enhancement of Abs and IQE, the EQE reaches the maximum value up to 44 ± 2.4‰ at 10%Cr^{3+} (Figure S18, Supporting Information), which is an outstanding result among the reported NIR phosphors.

It is quite interesting that the sintering technology greatly enhances the performance of the GGAG:Cr^{3+} material but is accompanied by the $GdBO_3$ impurity, in addition to the main garnet phase (Figures S17 and S19a, Supporting Information). This means that the effect of GdBO3 on reducing the luminescence of GGG:Cr^{3+} could be negligible. Because there is no site suitable for Cr^{3+} in the GdBO3 lattice. The percentages of the garnet phase monotonously increase while the $GdBO_3$ impurity is depressed with increasing Cr^{3+} concentrations (Figure S19b, Supporting Information). We try our best to reveal an interesting enhancement. The DR spectra from 800 to 1400 nm are flat, indicating that there is no Cr^{4+} for all samples (Figures S7 and S20, Supporting Information).[8,28] The absorption and luminescence should be from Cr^{3+}. The X-ray photoelectron spectroscopy (XPS) spectra confirm that the peaks at 575.0 and 575.4 eV belonging to the 2p orbital of Cr^{3+} are only observed (Figure S21, Supporting Information).[8,47] The XPS and EDS results reveal that the concentration of Cr^{3+} in experiment is lower than that in the nominal composition of GGAG:20%Cr^{3+} sintered at 1650 °C (Tables S9

© 2023 Wiley-VCH GmbH

18638899, 2024, 3, Downloaded from https://onlinelibrary.wiley.com/doi/10.1002/lpor.202300608 by Cas-Changchun Institute Of Optics, Fine Mechanics And Physics, Wiley Online Library on [18/04/2024]. See the Terms and Conditions (https://onlinelibrary.wiley.com/terms-and-conditions) on Wiley Online Library for rules of use; OA articles are governed by the applicable Creative Commons License

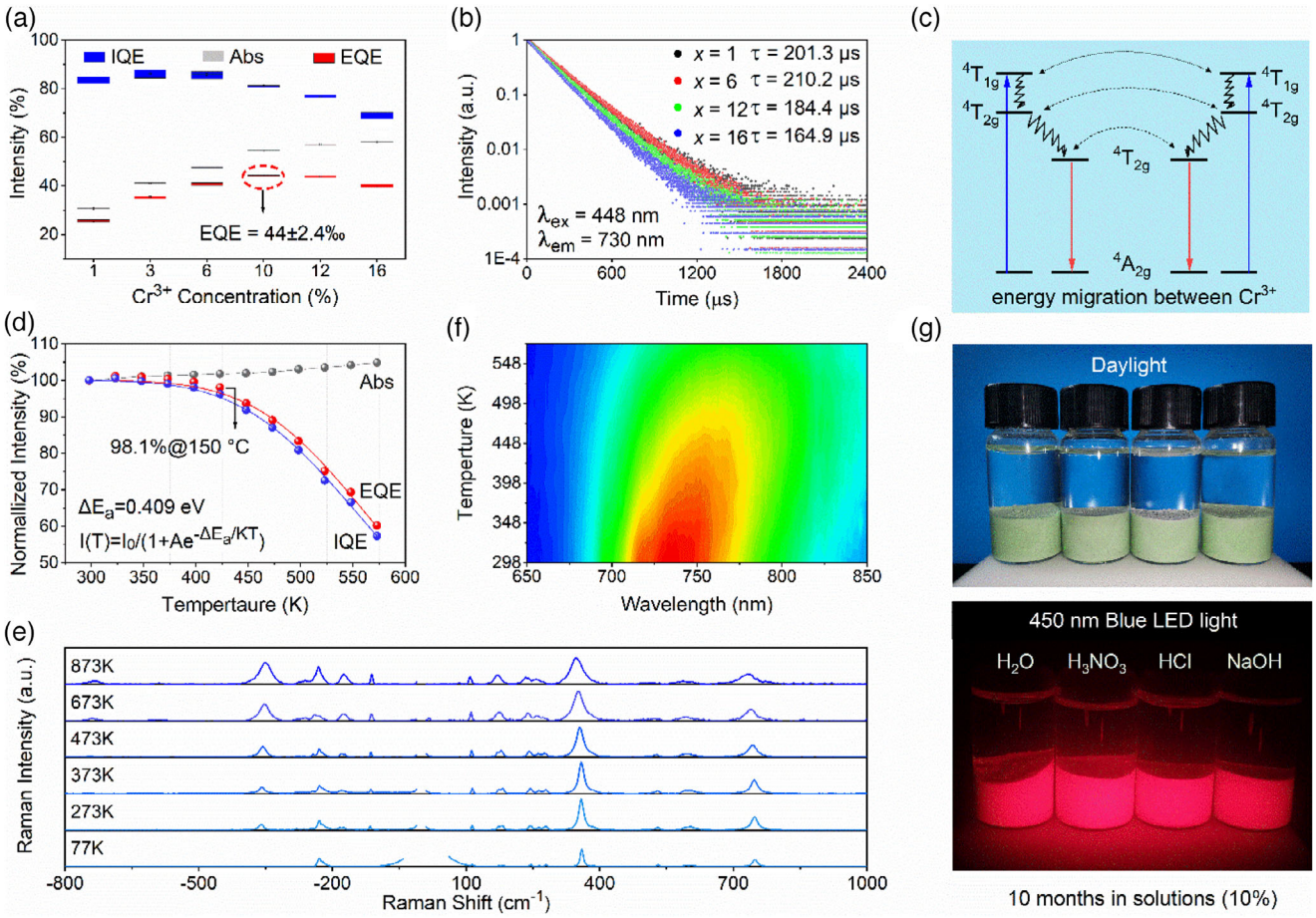

Figure 2. Efficiency, thermal, and environmental stability. a,b) EQE, IQE, and Abs as well as fluorescent decay curves and lifetimes for GGAG:xCr^{3+} (x = 1–16%). c) Simplified non-radiative relaxation schematic (dash lines). Energy migrations between Cr^{3+} lead to concentration quenching. d–f) Temperature-dependent EQE, IQE, and Abs (normalized), Raman spectra, and PL spectra of the optimized GGAG:10%Cr^{3+}. g) GGAG:10%Cr^{3+} powder samples immersed into water, or 10 vol% solutions of H_3NO_3, HCl, or NaOH for ten months. The NIR phosphors are green under daylight and are environmentally stable. Phosphors still show bright red light irradiated by the 450 nm blue LED.

and S10, Supporting Information). This could indicate that the Cr^{3+} evaporation is possible at a high temperature. The evaporation could be weakened when the sintering temperature declines from 1650 to 1350 °C by adding the H_3BO_3 flux (Table S11, Supporting Information). The Cr^{3+} could be easy to reach saturation and this is the possible reason why the optimal Cr^{3+} concentration is lowered to 10%. Thus, the interesting enhancement could be the comprehensive effects of crystallinity, Abs, and IQE at the lower Cr^{3+} concentration. The little Cr^{3+} concentration guarantees high thermal stability as well.

2.4. Excellently Thermal and Environmental Stability

The EQEs of the optimized GAGG:10%Cr^{3+} dependent on temperatures reveal excellent thermal stability. The EQEs almost consistent and display nearly zero thermal quenching from RT up to 400 K (Figure 2d; Figure S22, Supporting Information). Only small thermal quenching begins at 423 K, and the EQE maintains as high as 98.1% of the initial value at RT (Figure 2d). These results demonstrate greater thermal stability than the most of reported NIR phosphors (Table S12, Supporting Information).[8,27,32,48] The thermal quenching is only caused by the declined IQE due to the strengthened non-radiative relaxation at high temperatures.[8,49–51] The non-radiative relaxation includes the energy migrations among Cr^{3+} ions (Figure 2c), and electrons from the single Cr^{3+} ion reach the quenching point by overcoming the thermal barrier with an activation energy ΔE_a = 0.409 eV (fitted by the Arrhenius formula insert in Figure 2d).[8,49,51] The high activated energy also means that electrons are hard to reach the quenching point, and then Cr^{3+} manifests excellent thermal stability in the GGAG host. The slightly strengthened Cr^{3+} Abs with increasing temperatures contributes to the excellent thermal stability as well. It is noted that the temperature-dependent Raman spectra reveal broadened and strengthened vibrations (77–873 K, Figure 2e). These indicate that the thermal energy promotes asymmetric vibrations to break the d–d parity forbidden transitions of Cr^{3+}. Thus, as the temperature rises, the Abs into blue light from the $^4A_{2g} \rightarrow {}^4T_{1g}$ transition is enhanced due to the assisting of thermal phonons. Thermal phonons also strengthen the EPC and then the FWHM of the $^4T_{1g} \rightarrow {}^4A_{2g}$ NIR emission band broadens from 100 to 140 nm in the

© 2023 Wiley-VCH GmbH

18638899, 2024, 3, Downloaded from https://onlinelibrary.wiley.com/doi/10.1002/lpor.202300608 by Cas-Changchun Institute Of Optics, Fine Mechanics And Physics, Wiley Online Library on [18/04/2024]. See the Terms and Conditions (https://onlinelibrary.wiley.com/terms-and-conditions) on Wiley Online Library for rules of use; OA articles are governed by the applicable Creative Commons License

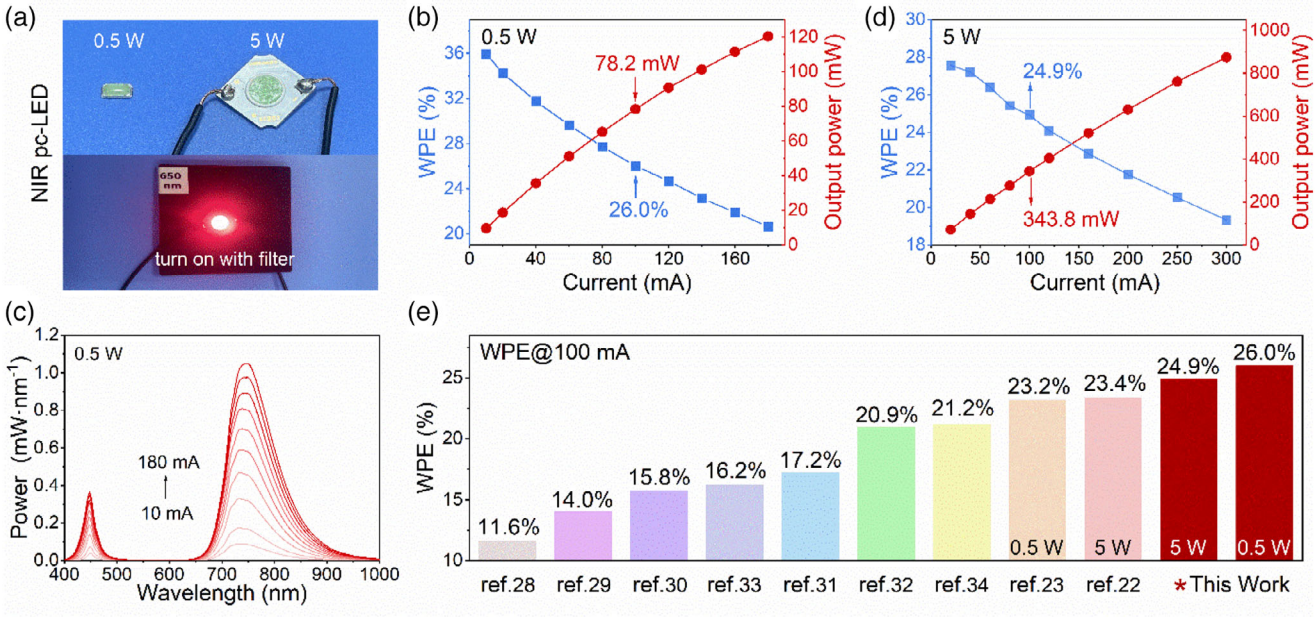

Figure 3. Performance of NIR pc-LEDs. a) Photographs of fabricated tiny (0.5 W) and high-power (5 W) NIR pc-LEDs using GGAG:10%Cr^{3+} phosphors and 450 nm blue chips. The turn-on device masking by a 650 nm long-pass filter shows red light. b) Emission spectra of the 0.5 W NIR pc-LED driven from 10 to 180 mA. c,d) Output NIR power and WPE of tiny and high-power NIR pc-LEDs dependent on driven currents. e) Progresses and comparison of WPEs for recent NIR pc-LEDs.

temperature-dependent PL spectra (Figure 2f; Figure S23, Supporting Information). In addition, the NIR emission peak redshifts from 730 to 772 nm (the shift energy ≈745 cm^{-1}). This phenomenon could mainly result from the weakened crystal-field strength aroused by the lattice expansion at a high temperature.[8]

The optimized GGAG:Cr^{3+} powder samples manifest good chemical and environmental stability. There is no distinct deterioration when the powders are immersed in water and varying solutions including 10 vol% H_3NO_3, 10 vol% HCl, or 10 vol% NaOH (Figure 2g). All the samples still show intense red light ten months later. The EQE, IQE, and Abs almost maintain in stable values when the samples have been placed in ambient humidity and temperature for three years (Figure S24, Supporting Information). We reproduced the samples several times. Essentially identical spectra properties for all systems demonstrate the reproducibility (Figure S25, Supporting Information).

2.5. High Performance of NIR Pc-LEDs

NIR pc-LEDs are manufactured by using the reproduced GGAG:10%Cr^{3+} phosphors and commercial 450 nm blue LEDs. Tiny (0.5 W) and high-power (5 W) devices are presented in **Figure 3**a. The devices show two emission bands at 450 and 730–740 nm, coming from the bluechip and the phosphor, respectively (Figure 3b; Figure S26, Supporting Information). The NIR emission in the spectra is strengthened as the driven current. For the tiny device, the output NIR power climbs from 9.6 to 120.4 mW with increasing the driven current from 10 to 180 mA (Figure 3c; Table S13, Supporting Information). The WPE declines from 36.0% to 20.6%. The efficiency of the blue LED drops from 77.6% to 44.4% when the driven current increases from 10 to 200 mA (Figure S27, Supporting Information). The droop tendency of the NIR pc-LED is similar to that of the blue LED. Thus, the efficiency droop is mainly from the intrinsic characteristic of LED chips, in addition to the phosphor degradation.[23] For the high-power device, the radiative NIR power rises from 71.7 to 873.9 mW as the current climbs from 20 to 300 mA, while the WPE droops from 27.6 to 19.3% (Figure 3d; Table S14, Supporting Information).

Usually, high-power LED devices suffer from severe thermal issues. Benefiting from the high efficiency and remarkable thermal stability of the developed NIR phosphor, it is significant that both the tiny and high-power devices show the best performance reported so far (Table S15, Supporting Information). The contrast WPE values at 100 mA are further represented in Figure 3e. For instance, the high-power device (5 W) has the same chip size,[22,32] and the achieved WPE of 24.9% is higher than those of 23.4% (based on CaO:Eu^{2+})[22] and 20.9% (based on Na_3ScF_6:Cr^{3+}).[32] The tiny device (0.5 W) has the same chip size,[23,30] and the achieved WPE of 26.0% is higher than those of 23.2% (based on $CaLu_2Mg_2Si_3O_{12}$:Cr^{3+})[23] and 15.8% (based on $Ca_2LuHf_2Al_3O_{12}$:Cr^{3+}).[30]

2.6. Applications

The high-efficiency and powerful NIR emission from the unprecedented NIR pc-LEDs partly matches with the far-red phytochrome (P_{fr}, Figure S28, Supporting Information), indicating the promising application in plant growth.[9,38,52] Beyond the above applications including night vision system,[22] food monitoring,[6,7] and so on. The absorption bands of Hb (deoxyhemoglobin) and HbO_2 (oxyhemoglobin) from 600 to 1000 nm.[53]

© 2023 Wiley-VCH GmbH

18638899, 2024, 3, Downloaded from https://onlinelibrary.wiley.com/doi/10.1002/lpor.202300608 by Cas-Changchun Institute Of Optics, Fine Mechanics And Physics, Wiley Online Library on [18/04/2024]. See the Terms and Conditions (https://onlinelibrary.wiley.com/terms-and-conditions) on Wiley Online Library for rules of use; OA articles are governed by the applicable Creative Commons License

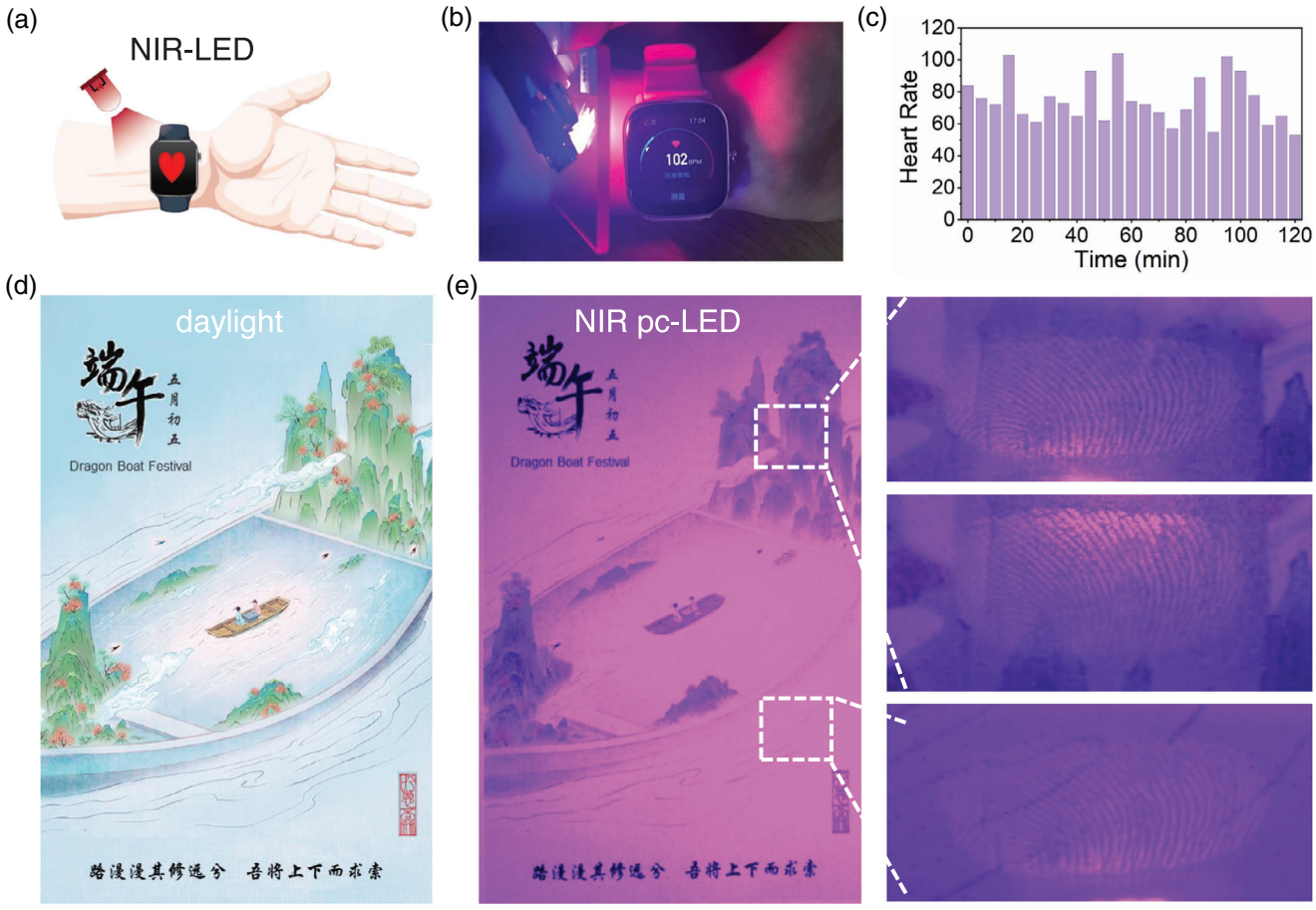

Figure 4. Applications of NIR pc-LEDs. a,b) Schematic diagram and demonstrations of the fabricated NIR pc-LED for heart rate monitoring by employing a smartwatch as the PPG detection at the wrist. c) Heart rate distributions in 2 h demonstrate the real-time monitoring function. d,e) Photographs of a fingerprinted painting taken under daylight and the NIR pc-LED light. The fingerprints are identified clearly under the NIR light.

The fabricated NIR pc-LED emits light in a broad range from 650 to 850 nm, with a peak at 730–740 nm. This overlaps partly with the absorption bands of Hb and HbO_2. Therefore, we extended it to heart rate detection technology, which has been commonly used in real-time health monitoring in wearable devices. For instance, smartwatches employ the green (530 nm) probing light and the photoplethysmography (PPG) measurement to detect heart rate (Figure S29, Supporting Information). The heart-rate function is out of work after masking black tapes on the green and red lights in a smartwatch (Video S1, Supporting Information). Then the masked smartwatch is used as the PPG detection. The schematic NIR probe-detection configuration is displayed in **Figure** 4a. We add the manufactured NIR pc-LEDs diagonally above the masked smartwatch and retrieve the heart rate through the PPG probe using the reflective principle. Heart rate detection could be realized well at the wrist and the neck of a volunteer (Figure 4b; Figure S30 and Video S2, S3, Supporting Information). We repeat the measurement 24 times at five-minute intervals (Figure 4c). Reliable heart rate detection demonstrates that the implemented NIR pc-LED has a promising application in real-time health monitoring. The monitoring is a reflection mode using the NIR pc-LED. The NIR probing light has a deep penetration depth into the skin and a reduced background signal from the environment. This may enlighten the development of a remote PPG technology for convenient heart rate detection and make contributions to health monitoring by a non-contract mode in terrible viral pneumonia cases on the globe. Furthermore, we extend the NIR pc-LEDs to fingerprint recognition (Figure 4d,e). Differing from the traditional technology coating luminescent materials,[54] the fingerprint can be immediately identified under the NIR pc-LED light (Figure 4e).

3. Conclusion

In summary, we have developed a strategy for achieving top-performance Cr^{3+}-activated NIR phosphors. Based on the preference occupation of Al in the GGG garnet, we introduce asymmetric vibrations by lattice distortions to break the d–d parity forbidden transitions of Cr^{3+} and then greatly promote its absorption and quantum efficiencies. To the best of our knowledge, the achieved NIR phosphor with an EQE over 44% and a thermal stability of more than 98% at 150 °C is the best comprehensive performance. The easy synthesis condition as well as chemical and environmental stability facilitate the reproduction and manufacture. The high efficiency and outstanding thermal

© 2023 Wiley-VCH GmbH

18638899, 2024, 3, Downloaded from https://onlinelibrary.wiley.com/doi/10.1002/lpor.202300608 by Cas-Changchun Institute Of Optics, Fine Mechanics And Physics, Wiley Online Library on [18/04/2024]. See the Terms and Conditions (https://onlinelibrary.wiley.com/terms-and-conditions) on Wiley Online Library for rules of use; OA articles are governed by the applicable Creative Commons License

stability enable us to achieve NIR pc-LEDs with the highest WPE of 26%@100 mA reported so far. Thus, we believe that the developed NIR phosphor can be a promising commercial candidate and pave the way for the realization of outstanding NIR pc-LEDs. In addition to traditional night vision-related fields, real-time heart rate detection and fingerprint recognition provide proof-of-concept tests of the promising prospects of health and information monitoring for the first time. Our work may open up a range of exciting applications from high-performance NIR luminescent materials to smart NIR light sources.

4. Experimental Section

Raw Materials and Synthesis of Phosphors: Gd_2O_3 (99.9%), Al_2O_3 (99.9%), Gd_2O_3 (99.9%), Cr_2O_3 (99.95%), and H_3BO_3 were purchased from Aladdin. Raw materials were weighed according to nominal compositions, mixed, and grounded in an agate mortar for 30 min, then loaded into an aluminum oxide crucible and synthesized by a high-temperature solid-state reaction in an air atmosphere. Samples with the nominal composition of $Gd_3Ga_{4-x}AlO_{12}:xCr^{3+}$ ($x = 5-30\%$) were sintered at 1650 °C for 3 h. Samples with the nominal composition of $Gd_3Ga_{4-x}AlO_{12}:xCr^{3+}$ ($x = 1-16\%$) and 3wt% H_3BO_3 were sintering at 1350 °C for 2 h confirmed by the orthogonal experiment. This means first fixing the Cr^{3+} concentration at 10% and optimizing the H_3BO_3 concentration. The optimal value was 3 wt.% for H_3BO_3. Then fix the H_3BO_3 concentration at 3 wt.% and optimize the Cr^{3+} concentration. The optimal value for Cr^{3+} was 10%. The sintered samples were cooled down to room temperature and ground to powders for characterizations.

Fabrication of NIR Pc-LEDs: NIR pc-LEDs were fabricated using the optimized GGAG:10%Cr^{3+} + 3wt.% H_3BO_3 phosphors mixed with transparent epoxy resin. The mixtures with a mass ratio of the epoxy resin to phosphors of 3:2 were encapsulated on the tiny blue LED chips (2835 type, 450 nm, 0.5 W, from Shenzhen Chaoyue Optoelectronic Co., Ltd, China) for madding tiny NIR pc-LEDs. The mass ratio was 5:3 for madding high-power NIR pc-LEDs using the chip-on-board blue LED (X1901, 450 nm, 5 W, from Guangzhou LEDteen Optoelectronics Co., Ltd., China).

Characterization: X-ray diffraction (XRD) patterns were measured by a Bruker D8 X-ray diffractometer with Cu Kα radiation (λ = 1.54056 Å) at 40 kV and 40 mA. Rietveld refinements of XRD profiles were performed by using the general structure analysis system (GSAS) program. Diffuse reflectance (DR) spectra were measured by a LAMBDA 950. X-ray photoelectron spectroscopy (XPS) was performed on a Kratos Axis Ultra DLD. Raman spectra were recorded with a LabRam spectrometer (LabRam Odyssey, HORIBA FRANCE SAS) using 532 nm Nd-YAG laser and ultra-low wavenumber accessory as the excitation source at 77–873 K. A field-emission scanning electron microscope (FE-SEM, Hitachi S-4800) equipped with an energy dispersive X-ray spectroscopy (EDS) system and a cathodoluminescence (CL) system (MonoCL4, Gatan) was used to measure the morphology, elements, and CL spectra. High-angle annular dark field (HAADF)-scanning transmission electron microscopy (STEM) were conducted by using a double spherical aberration corrected Spectra 300 TEM (ThermoFisher company, USA) at 300 kV acceleration voltage. Photoluminescence (PL) spectra from 650 to 900 nm at room temperature (RT) were recorded by a Hitachi F-4600 spectrometer. PL and PLE spectra at RT and 77 K (by dipping the sample in liquid nitrogen) and fluorescence decay curves were measured by a Horiba FL-311 spectrometer. Internal quantum efficiency (IQE), external quantum efficiency (EQE), and absorbance (Abs.) were recorded by an Otsuka Photal Electronics QE-2100 system from RT–573 K. $BaSO_4$ powder was used for calibration. The excitation wavelength is 448 nm. The IQE, EQE, and Abs. of the optimized GGAG:10%Cr^{3+} at RT were remeasured by a UV–NIR absolute photoluminescence quantum yield spectrometer (Quantaurus-QY Plus C13534-12, Hamamatsu Photonics) for confirming the results (listed in Table S16, Supporting Information). The calculated EQE reached 43.9 ± 0.6%, which was close to 44±2.4‰ recorded by an Otsuka Photal Electronics QE-2100 system. The photoelectric properties of NIR pc-LED devices including the electroluminescence spectra and photoelectric efficiency were characterized on an integrated photoelectric measurement system (LHS-1000, EVERFINE), which was equipped with an array spectrophotometer (350–1100 nm, HAAS-2000) and an integrating sphere (SPEKTRON R98, Φ 50 cm). The application of real-time heart rate detection was taken by a wearable device (GTS2 mini, Amazfit) as a PPG system. The videos were recorded by a smartphone (Huawei Nova 5 Pro). The fingerprint was from a volunteer. The picture was re-created based on the image from "hucongmisuan" and "renminchuangyi". The photographs were taken by a digital camera (Canon EOS 80D).

Supporting Information

Supporting Information is available from the Wiley Online Library or from the author.

Acknowledgements

This work was supported by the National Natural Science Foundation of China (12074393), "Pioneer" and "Leading Goose" R&D Program of Zhejiang (2022C01046), and the Youth Innovation Promotion Association Chinese Academy of Sciences (2021295). The authors thank E. Song from the South China University of Technology for fabricating and measuring the high-power NIR pc-LEDs. Informed consent was obtained from the volunteer (the first author) for recording the heart rate.

Conflict of Interest

The authors declare no conflict of interest.

Data Availability Statement

The data that support the findings of this study are available from the corresponding author upon reasonable request.

Keywords

Cr^{3+}, garnet, NIR phosphor, NIR pc-LED light, heart-rate detection

Received: July 3, 2023
Revised: October 18, 2023
Published online: December 12, 2023

[1] F. Zhao, Z. Song, Q. Liu, *Laser Photonics Rev.* **2022**, *16*, 2200380.
[2] H. Zhang, G. Wang, Z. Zhang, J. H. Lei, T.-M. Liu, G. Xing, C.-X. Deng, Z. Tang, S. Qu, *Light: Sci. Appl.* **2022**, *11*, 113.
[3] D. Liu, G. Li, P. Dang, Q. Zhang, Y. Wei, L. Qiu, H. Lian, M. Shang, J. Lin, *Light: Sci. Appl.* **2023**, *12*, 248.
[4] Z. Lv, L. Jin, Y. Cao, H. Zhang, D. Xue, N. Yin, T. Zhang, Y. Wang, J. Liu, X. Liu, H. Zhang, *Light: Sci. Appl.* **2022**, *11*, 116.
[5] H. Suo, Y. Wang, X. Zhao, X. Zhang, L. Li, K. Guan, W. Ding, P. Li, Z. Wang, F. Wang, *Laser Photon. Rev.* **2022**, *16*, 2200012.
[6] C. Dincer, R. Bruch, E. Costa-Rama, M. T. Fernández-Abedul, A. Merkoçi, A. Manz, G. A. Urban, F. Güder, *Adv. Mater.* **2019**, *31*, 1806739.
[7] X. Chen, Y. Li, K. Huang, L. Huang, X. Tian, H. Dong, R. Kang, Y. Hu, J. Nie, J. Qiu, G. Han, *Adv. Mater.* **2021**, *33*, 2008722.

© 2023 Wiley-VCH GmbH

18638899, 2024, 3, Downloaded from https://onlinelibrary.wiley.com/doi/10.1002/lpor.202300608 by Cas-Changchun Institute Of Optics, Fine Mechanics And Physics, Wiley Online Library on [18/04/2024]. See the Terms and Conditions (https://onlinelibrary.wiley.com/terms-and-conditions) on Wiley Online Library for rules of use; OA articles are governed by the applicable Creative Commons License

[8] Z. Jia, C. Yuan, Y. Liu, X.-J. Wang, P. Sun, L. Wang, H. Jiang, J. Jiang, *Light: Sci. Appl.* **2020**, *9*, 86.
[9] Y. Xiao, W. Xiao, D. Wu, L. Guan, M. Luo, L.-D. Sun, *Adv. Funct. Mater.* **2022**, *32*, 2109618.
[10] J. Sun, W. Zheng, P. Huang, M. Zhang, W. Zhang, Z. Deng, S. Yu, M. Jin, X. Chen, *Angew. Chem., Int. Ed.* **2022**, *134*, e202201993.
[11] J. Lu, X. Guan, Y. Li, K. Lin, W. Feng, Y. Zhao, C. Yan, M. Li, Y. Shen, X. Qin, Z. Wei, *Adv. Mater.* **2021**, *33*, 2104414.
[12] M. Vasilopoulou, A. Fakharuddin, F. P. García De Arquer, D. G. Georgiadou, H. Kim, A. R. B. Mohd Yusoff, F. Gao, M. K. Nazeeruddin, H. J. Bolink, E. H. Sargent, *Nat. Photon.* **2021**, *15*, 656.
[13] A. Minotto, P. A. Haigh, L. G. Lukasiewicz, E. Lunedei, D. T. Gryko, I. Darwazeh, F. Cacialli, *Light: Sci. Appl.* **2020**, *9*, 70.
[14] C. Cai, S. Liu, F. Zhao, H. Cai, Z. Song, Q. Liu, *J. Mater. Chem. C* **2023**,*11*, 8462.
[15] D. Wen, H. Liu, Y. Guo, Q. Zeng, M. Wu, R.-S. Liu, *Angew. Chem., Int. Ed.* **2022**, *134*, e202204411.
[16] Y. Jin, Z. Zhou, R. Ran, S. Tan, Y. Liu, J. Zheng, G. Xiang, L. Ma, X.-J. Wang, *Adv. Optical Mater.* **2022**, *10*, 2202049.
[17] G. Huang, Y. Liu, D. Wang, Y. Zhu, S. Wen, J. Ruan, D. Jin, *eLight* **2022**, *2*, 20.
[18] D. Hayashi, A. M. Van Dongen, J. Boerekamp, S. Spoor, G. Lucassen, J. Schleipen, *Appl. Phys. Lett.* **2017**, *110*, 233701.
[19] J. Qiao, G. Zhou, Y. Zhou, Q. Zhang, Z. Xia, *Nat. Commun.* **2019**, *10*, 5267.
[20] J. J. Joos, D. Van Der Heggen, L. I. D. J. Martin, L. Amidani, P. F. Smet, Z. Barandiarán, L. Seijo, *Nat. Commun.* **2020**, *11*, 3647.
[21] S. Liu, H. Cai, S. Zhang, Z. Song, Z. Xia, Q. Liu, *Mater. Chem. Front.* **2021**, *5*, 3841.
[22] J. Qiao, S. Zhang, X. Zhou, W. Chen, R. Gautier, Z. Xia, *Adv. Mater.* **2022**, *34*, 2201887.
[23] H. Xiao, J. Zhang, L. Zhang, H. Wu, H. Wu, G. Pan, F. Liu, J. Zhang, *Adv. Opt. Mater.* **2021**, *9*, 2101134.
[24] S. Pradhan, F. Di Stasio, Y. Bi, S. Gupta, S. Christodoulou, A. Stavrinadis, G. Konstantatos, *Nature Nanotech* **2019**, *14*, 72.
[25] D. Liu, G. Li, P. Dang, Q. Zhang, Y. Wei, L. Qiu, M. S. Molokeev, H. Lian, M. Shang, J. Lin, *Light: Sci. Appl.* **2022**, *11*, 112.
[26] Y. Zhang, S. Miao, Y. Liang, C. Liang, D. Chen, X. Shan, K. Sun, X.-J. Wang, *Light: Sci. Appl.* **2022**, *11*, 136.
[27] D. Huang, H. Zhu, Z. Deng, H. Yang, J. Hu, S. Liang, D. Chen, E. Ma, W. Guo, *J. Mater. Chem. C* **2021**, *9*, 164.
[28] R. Li, Y. Liu, C. Yuan, G. Leniec, L. Miao, P. Sun, Z. Liu, Z. Luo, R. Dong, J. Jiang, *Adv. Opt. Mater.* **2021**, *9*, 2100388.
[29] E. T. Basore, W. Xiao, X. Liu, J. Wu, J. Qiu, *Adv. Opt. Mater.* **2020**, *8*, 2000296.
[30] L. Zhang, D. Wang, Z. Hao, X. Zhang, G.-H. Pan, H. Wu, J. Zhang, *Adv. Opt. Mater.* **2019**, *7*, 1900185.
[31] X. Xu, Q. Shao, L. Yao, Y. Dong, J. Jiang, *Chem. Eng. J.* **2020**, *383*, 123108.
[32] F. He, E. Song, Y. Zhou, H. Ming, Z. Chen, J. Wu, P. Shao, X. Yang, Z. Xia, Q. Zhang, *Adv. Funct. Mater.* **2021**, *31*, 2103743.
[33] G. Zheng, W. Xiao, H. Wu, J. Wu, X. Liu, J. Qiu, *Laser Photon. Rev.* **2021**, *15*, 2100060.
[34] G. Zheng, W. Xiao, J. Wu, X. Liu, H. Masai, J. Qiu, *Adv. Sci.* **2022**, *9*, 2105713.
[35] Q. Yao, P. Hu, P. Sun, M. Liu, R. Dong, K. Chao, Y. Liu, J. Jiang, H. Jiang, *Adv. Mater.* **2020**, *32*, 1907888.
[36] B. Struve, G. Huber, *Appl. Phys. B* **1985**, *36*, 195.
[37] M. Mao, T. Zhou, H. Zeng, L. Wang, F. Huang, X. Tang, R.-J. Xie, *J. Mater. Chem. C* **2020**, *8*, 1981.
[38] A. Zabiliute, S. Butkute, A. Zukauskas, P. Vitta, A. Kareiva, *Appl. Opt.* **2014**, *53*, 907.
[39] A. Nakatsuka, A. Yoshiasa, T. Yamanaka, *Acta Cryst. B* **1999**, *55*, 266.
[40] V. Laguta, Y. Zorenko, V. Gorbenko, A. Iskaliyeva, Y. Zagorodniy, O. Sidletskiy, P. Bilski, A. Twardak, M. Nikl, *J. Phys. Chem. C* **2016**, *120*, 24400.
[41] C. Milanese, V. Buscaglia, F. Maglia, U. Anselmi-Tamburini, *Chem. Mater.* **2004**, *16*, 1232.
[42] B. Malysa, A. Meijerink, T. Jüstel, *J. Lumin.* **2018**, *202*, 523.
[43] H. Jiang, L. Chen, G. Zheng, Z. Luo, X. Wu, Z. Liu, R. Li, Y. Liu, P. Sun, J. Jiang, *Adv. Optical Mater.* **2022**, *10*, 2102741.
[44] Z. Pan, Y.-Y. Lu, F. Liu, *Nat. Mater.* **2012**, *11*, 58.
[45] T. Maldiney, A. Bessière, J. Seguin, E. Teston, S. K. Sharma, B. Viana, A. J. J. Bos, P. Dorenbos, M. Bessodes, D. Gourier, D. Scherman, C. Richard, *Nat. Mater.* **2014**, *13*, 418.
[46] M. Back, J. Ueda, M. G. Brik, S. Tanabe, *ACS Appl. Mater. Interfaces* **2020**, *12*, 38325.
[47] Z. Shadike, Y.-N. Zhou, L.-L. Chen, Q. Wu, J.-L. Yue, N. Zhang, X.-Q. Yang, L. Gu, X.-S. Liu, S.-Q. Shi, Z.-W. Fu, *Nat. Commun.* **2017**, *8*, 566.
[48] V. Rajendran, M.-H. Fang, W.-T. Huang, N. Majewska, T. Lesniewski, S. Mahlik, G. Leniec, S. M. Kaczmarek, W. K. Pang, V. K. Peterson, K.-M. Lu, H. Chang, R.-S. Liu, *J. Am. Chem. Soc.* **2021**, *143*, 19058.
[49] M. Liu, Q. Wan, H. Wang, F. Carulli, X. Sun, W. Zheng, L. Kong, Q. Zhang, C. Zhang, Q. Zhang, S. Brovelli, L. Li, *Nat. Photon.* **2021**, *15*, 379.
[50] P. Qi, Y. Luo, B. Shi, W. Li, D. Liu, L. Zheng, Z. Liu, Y. Hou, Z. Fang, *eLight* **2021**, *1*, 6.
[51] K. Zhao, X. Xu, W. Ren, D. Jin, P. Xi, *eLight* **2022**, *2*, 5.
[52] X, Zou, X.-J. Wang, H. Zhang, Y. Kang, X. Yang, X. Zhang, M. S. Molokeev, B. Lei, *Chem. Eng. J.* **2022**, *428*, 132003.
[53] J. H. Kim, A. Liess, M. Stolte, A.-M. Krause, V. Stepanenko, C. Zhong, D. Bialas, F. Spano, F. Würthner, *Adv. Mater.* **2021**, *33*, 2100582.
[54] M.-H. Fang, K.-C. Chen, N. Majewska, T. Lesniewski, S. Mahlik, G. Leniec, S. M. Kaczmarek, C.-W. Yang, K.-M. Lu, H.-S. Sheu, R.-S. Liu, *ACS Energy Lett.* **2021**, *6*, 109.

© 2023 Wiley-VCH GmbH

18638899, 2024, 3, Downloaded from https://onlinelibrary.wiley.com/doi/10.1002/lpor.202300608 by Cas-Changchun Institute Of Optics, Fine Mechanics And Physics, Wiley Online Library on [18/04/2024]. See the Terms and Conditions (https://onlinelibrary.wiley.com/terms-and-conditions) on Wiley Online Library for rules of use; OA articles are governed by the applicable Creative Commons License